Journal of Sensor Science and Technology
Vol. 33, No. 5 (2024) pp. 274-287
http://dx.doi.org/10.46670/JSST.2024.33.5.274
pISSN 1225-5475/eISSN 2093-7563

Photoactivated Metal Oxide-based Chemiresistors: Revolutionizing Gas Sensing with Ultraviolet Illumination

Sunwoo Lee[1,*], Gye Hyeon Lee[1,*], Myungwoo Choi[2,*], Gana Park[1], Dakyung Kim[3], Sangbin Lee[3], Jeong-O Lee[1,+], and Donghwi Cho[1,4,+]

Abstract

Chemiresistors play a crucial role in numerous research fields, including environmental monitoring, healthcare, and industrial safety, owing to their ability to detect and quantify gases with high sensitivity and specificity. This review provides a comprehensive overview of the recent advancements in photoactivated chemiresistors and emphasizes their potential for the development of highly sensitive, selective, and low-power gas sensors. This study explores a range of structural configurations of sensing materials, from zero-dimensional quantum dots to three-dimensional, porous nanostructures and examines the impact of these designs on the photoactivity, gas interactions, and overall sensor performance—including gas responses and recovery rates. Particular focus is placed on metal-oxide semiconductors and the integration of ultraviolet micro-light emitting diodes, which have gained attention as key components for next-generation sensing technologies owing to their superior photoactivity and energy efficiency. By addressing existing technical challenges, such as limited sensitivity, particularly at room temperature (~22°C), this paper outlines future research directions, highlighting the potential of photoactivated chemiresistors in developing high-performance, ultralow-power gas sensors for the Internet of Things and other advanced applications.

Keywords: Photoactivated chemiresistors, Gas sensors, Metal oxide semiconductors, Nanostructure, μLEDs

1. INTRODUCTION

Chemical sensors have garnered significant attention across a broad range of research fields because of their ability to detect hazardous substances [1], monitor indoor and outdoor air quality [2], and contribute to advancements in healthcare [3,4]. These sensors are indispensable in various applications and provide critical data to ensure safety and human well-being. Among the various technologies developed for chemical sensing, oxide semiconductor-based sensors are the most prominent and effective. This technology is highly valued for its sensitivity, selectivity, and robustness, making it suitable for a wide array of sensing applications [5,6]. As technology continues to evolve, there is a growing demand for smaller and more integrated sensor devices that can be seamlessly incorporated into wearable electronics [7]. Such devices have the potential to revolutionize healthcare by enabling continuous monitoring of vital signs and environmental conditions—thus providing real-time data that could lead to the early detection of health issues and more personalized care. Despite considerable progress in oxide-semiconductor sensor technology, its integration into wearable healthcare devices has not yet reached its full potential.

The slow adoption of these sensors in wearable devices is attributed to several challenges. A primary obstacle is the high-power consumption associated with the conventional operation of oxide-semiconductor gas sensors. These sensors typically rely on thermal activation, which normally requires heating the sensing material to temperatures approaching 400°C. Although this method significantly improves sensor performance, it also introduces several challenges. High operational temperatures can degrade the surrounding electronic components, leading to potential reliability issues [8]. Additionally, the materials used in

[1]Thin Film Materials Research Center, Korea Research Institute of Chemical Technology
Daejeon 34114, Republic of Korea
[2]Department of Materials Science and Engineering, Korea University
Seoul 02841, Republic of Korea
[3]Energy Materials, University of Science of Technology and Education
Cheonan 31253, Republic of Korea
[4]Advanced Materials and Chemical Engineering, University of Science and Technology
Daejeon 34113, Republic of Korea
*These authors equally contributed to this manuscript.
[+]Corresponding author: jolee@krict.re.kr, roy.cho@krict.re.kr
(Received: Sep. 2, 2024, Revised: Sep. 9, 2024, Accepted: Sep. 13, 2024)

sensors may suffer from reduced durability owing to prolonged exposure to extreme temperatures. Furthermore, the need for thermal activation poses a major challenge for wearable applications, where energy efficiency and thermal safety are paramount. Despite notable developments in micro-heating technologies, wearable devices—which are often battery-powered—require sensors that can operate efficiently over extended periods without frequent recharging. The need for thermal insulation to protect the other components from heat further complicates the integration of these sensors into compact lightweight devices [9]. This additional insulation often results in bulkier systems that are less desirable for wearable electronics, where size and comfort are critical factors.

To overcome these challenges, researchers have explored alternative activation methods that can expand applicability without the drawbacks of thermal activation. A promising approach is photoactivation [10], in which light is used instead of heat to activate the sensing material. Photoactivated sensors have the potential to operate at room temperature (~22°C), reducing power consumption to the microwatt level, and eliminating the need for bulky thermal insulation [11]. This approach has the proven advantages of compact, energy-efficient configurations and high performance—suitable for integration into wearable healthcare monitoring systems [9].

In this review, we explore recent advancements in chemical sensing through photoactivation methods, highlighting their key requirements, such as material design (dimensions, periodicity, symmetry, etc.), nanostructures, and light sources. We also explore the emerging potential of photoactivation as a viable alternative and discuss its advantages and implications for future applications in wearable electronics. By addressing these critical issues, this review aims to provide a comprehensive overview of state-of-the-art, photoactivated, chemical-sensor technology compared to its thermal counterpart and highlight the pathways that could lead to the next generation of low-power, safe, and high-performance chemiresistors.

2. MECHANISM FOR THE PHOTOACTIVATION

Photoactivated gas sensors operate based on the photoelectric effect (when light impinges on the material photons are absorbed triggering photoelectron emission). When photons, with energy greater than or equal to the semiconductor bandgap ($h\nu \geq E_g$), collide with the electrons, they move up from the valence band to the conduction band, leaving behind holes. Fig. 1 (a) illustrates the widely accepted mechanism of chemiresistive gas sensing, involving oxygen absorbate-mediated electrical interactions. Depending on the temperature, oxygen (O_2) molecules adsorb onto semiconductor surfaces in different ionized states (O_2^-, O^-, or O^{2-}). Below 150°C, the molecular form O_2^- is predominant, while above 150°C, atomic forms O^-, or O^{2-} are more common [12]. Even at room temperature (~22°C), studies have shown ionized oxygen molecules ($O_{2(ads)}^-$) on semiconductor surfaces, evidenced by conductivity measurements in pure O_2 and nitrogen (N_2) environments without external heating or photoactivation [13].

Oxygen absorbate-mediated mechanisms are crucial for photoactivated gas sensors at room temperature (~22°C). In the absence of light, oxygen adsorption follows a conventional path in which molecular oxygen ($O_{2(ads)}^-$) binds to the surface. Photogenerated electrons and holes are produced under light irradiation. The holes ($h_{(photo)}^+$) interact with the adsorbed molecular oxygen ($O_{2(ads)}^-$), causing desorption and exposure of reactive sites, which enhances gas-sensing reactions by increasing the number of available sites.

Desorbed and (any) pre-existing oxygen react with photogenerated electrons ($e_{(photo)}^-$) and re-adsorb as molecular oxygen ($O_{2(gas)} + e_{(photo)}^- \rightarrow O_{2(photo)}^-$). These photoadsorbed oxygen molecules ($O_{2(photo)}^-$) are less strongly bound to the semiconductor and are more reactive than naturally ionosorbed oxygen ($O_{2(ads)}^-$), which is more stable and less reactive at room temperature (~22°C). Furthermore, the ultraviolet (UV)-induced localized surface-plasmon resonance (LSPR) effect enhances light absorption and generates local photothermal effects. This LSPR effect accelerates surface chemical-reaction kinetics by facilitating the movement of photoactive charge carriers [14]. Consequently, light irradiation enhances the overall gas-sensing kinetics and improves the sensor response.

For example, nitrogen dioxide (NO_2), a well-known oxidizing gas, reacts with photo-adsorbed oxygen, leading to electron withdrawal from the semiconductor, which increases the resistance in n-type semiconductors ($NO_2 + O_{2(photo)}^- \rightarrow NO_{2(ads)}^- + O_{2(gas)}$). Conversely, reducing gases like acetone (CH_3COCH_3) transfer electrons to the semiconductor, producing carbon dioxide (CO_2) and water (H_2O), ($CH_3COCH_3 + 4O_{2(photo)}^- \rightarrow 3CO_2 + 3H_2O + 4e^-$), resulting in a decrease in resistance in n-type semiconductors.

Among various semiconductor oxides, including zinc oxide (ZnO), tin oxide (SnO_2), tungsten trioxide (WO_3), diindium trioxide (In_2O_3), and titanium dioxide (TiO_2) (Fig. 1 (b)), photoelectrons are generated when exposed to UV light-emitting diode (LED) light under an applied voltage, leading to a

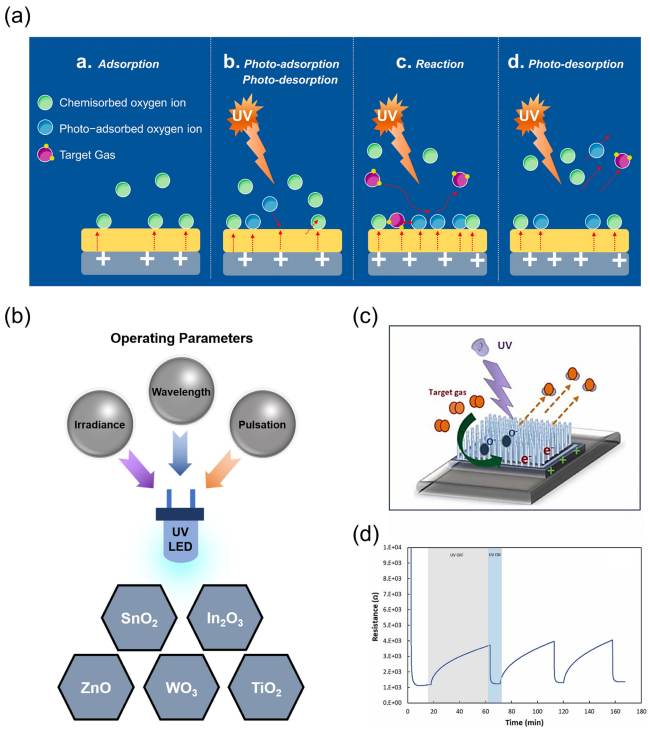

Fig. 1. (a) Photo-activated sensing mechanism under UV illumination. Reprinted with permission from Ref. [15] © 2023 by the authors. Licensee MDPI, Basel, Switzerland. (b) Materials commonly used as photo-activated materials. (c) Photo-activated sensing mechanism with target gas. (d) Time-dependent resistance measured at 5V bias at room temperature (~22°C), showing photo-response upon 275nm UV-LED on/off illumination. Reprinted with permission from Ref. [16] © 2024 The Authors. Published by Elsevier B.V.

significant drop in resistance; this fully recovers when the light source is removed. This photoresponse occurs rapidly, making these materials highly responsive to UV activation. Figs. 1 (c) and (d) illustrate the reaction of NO_2 gas with the n-type ZnO nanowires under UV light. UV exposure generates photoelectrons and holes on the ZnO sensor surface. This process has four steps as follows:

(1) At room temperature (~22°C), O_2 molecules adsorb onto the surface and

(2) react with photoelectrons and desorb as oxygen-ion species.

(3) Some also react with the photogenerated holes, desorbing them as O_2 molecules.

(4) Over time, equilibrium is reached between the electron-and-hole generation and oxygen-ion reactions. When exposed to NO_2 gas in a continuous UV environment, the gas reacts with electrons, reducing the electron count on the ZnO surface and increasing the sensor resistance.

Therefore, light sources with energies exceeding the bandgap of the semiconductor engage internal charge carriers in chemical reactions, accelerating interactions between the semiconductor and gas molecules. This enhances sensor performance, particularly under light irradiation, where gas sensing becomes faster and more efficient.

3. EFFECT OF STRUCTURAL DIMENSIONS ON PHOTOACTIVATED CHEMIRESISTORS

The structural dimensions of photoactivated gas-sensing materials significantly influence their performance, particularly in terms of light absorption, gas interactions, and overall physicochemical responses. In this section, we explore how different structural dimensions affect the efficacy of photoactive chemiresistors, focusing on how dimensional scaling affects sensor performance and characteristics.

3.1 0-Dimensional Photoactive Sensing Materials

Figs. 2(a) and (b) show the high ethanol (C_2H_5OH)-gas sensitivity of the UV-activated TiO_2 quantum dots at room temperature (~22°C). UV exposure generates holes that drive the photocatalytic oxidation of C_2H_5OH, leading to the elimination of these holes and influx of electrons into the conduction band [17-19]. This process alters the electrical and optical characteristics of TiO_2 nanoparticles. Under 365 nm UV light, electron-hole pairs are produced, and the subsequent removal of holes by C_2H_5OH gas results in the accumulation of electrons in the conduction band, as depicted in Fig. 2 (a). Fig. 2 (b) shows the resistance changes under three distinct conditions: (i) resistance variation due to UV exposure without C_2H_5OH, (ii) resistance variation due to 1,000 parts-per-million (ppm) C_2H_5OH exposure in the absence of UV light, and (iii) resistance variation due to 1,000 ppm C_2H_5OH exposure under UV illumination. Under condition (i), the UV-generated electrons in the conduction band cause a reduction in resistance, which is then recovered once the UV light is removed. In condition (ii), exposure to 1,000 ppm C_2H_5OH in the dark leads to an increase in resistance from 1.5×10^9 Ω to 1.17×10^{10} Ω, attributed to C_2H_5OH absorption in the sample film [20]. In condition (iii), exposure to C_2H_5OH under UV light causes a significant decrease in resistance from 1.1×10^9 Ω to 7.8×10^6 Ω. This indicates that the reaction mechanism is influenced by the presence of UV light, with the interaction between C_2H_5OH and electrons being more pronounced than C_2H_5OH absorption in the sample film in the presence of UV light.

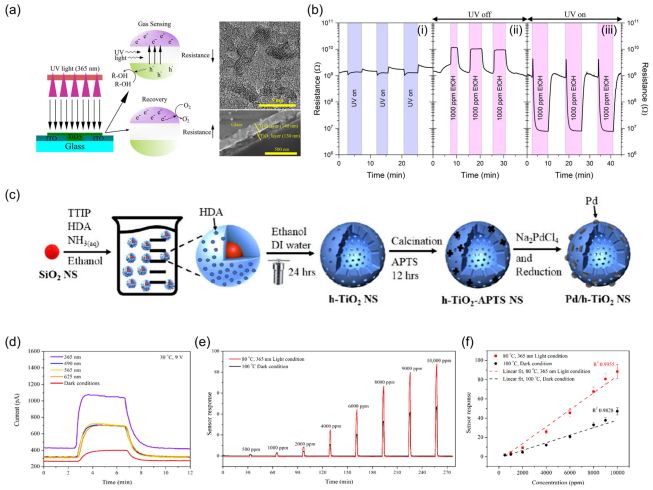

Fig. 2. (a) Gas sensing and recovery mechanisms of the TiO_2 UV gas sensor. (b) (i) Change in resistance when switching the UV light on and off without solvent gas at a flux density of 46 mW/cm²; (ii) change in resistance when adding C_2H_5OH (1,000 ppm) and ventilating the chamber without UV light; and (iii) change in resistance when adding C_2H_5OH (1,000 ppm) and ventilating the chamber while irradiating with UV light. Reprinted with permission from Ref. [21] © 2021 American Chemical Society. (c) Preparation process for h-TiO_2/Pd NS. (d) Pd/h-TiO_2 NS sensor current toward hydrogen with different light wavelengths at 30°C and 1,000 ppm hydrogen. (e) Pd/h-TiO_2 NS sensor response toward hydrogen (500–10,000 ppm). (f) Calibration curve for hydrogen (500–10,000 ppm) with 365 nm light at 80°C and under dark conditions at 100°C under a 9 V bias. Reprinted with permission from Ref. [22] © 2024 American Chemical Society

Fig. 2 (c) shows the fabrication process of hollow TiO_2 nanospheres (h-TiO_2 NS) with Pd nanoparticles deposited on their surfaces. The response of these Pd/h-TiO_2 NS structures to 1,000 ppm of hydrogen gas was evaluated under various wavelengths (365, 490, 565, and 625 nm) and dark conditions (Fig. 2 (d)). The wavelength of 365 nm was the most effective, showing a rapid response with a factor of 1.55. Fig. 2 (e) compares the hydrogen sensing performance at concentrations between 500 and 10,000 ppm under 365 nm UV light at 80°C and in dark conditions at 100°C. These data clearly demonstrate that UV irradiation significantly improves hydrogen detection. Additionally, the R^2 value calculated to assess linearity under 365 nm UV light at 80°C indicates a detection limit as low as 17 parts-per-billion (ppb) (Fig. 2 (f)).

3.2 1-Dimensional Photoactive Sensing Materials

Fig. 3 (a) shows the fabrication process of the gas sensors using TiO_2 nanoparticles (NPs), ZnO hemitubes (HTs), and ZnO

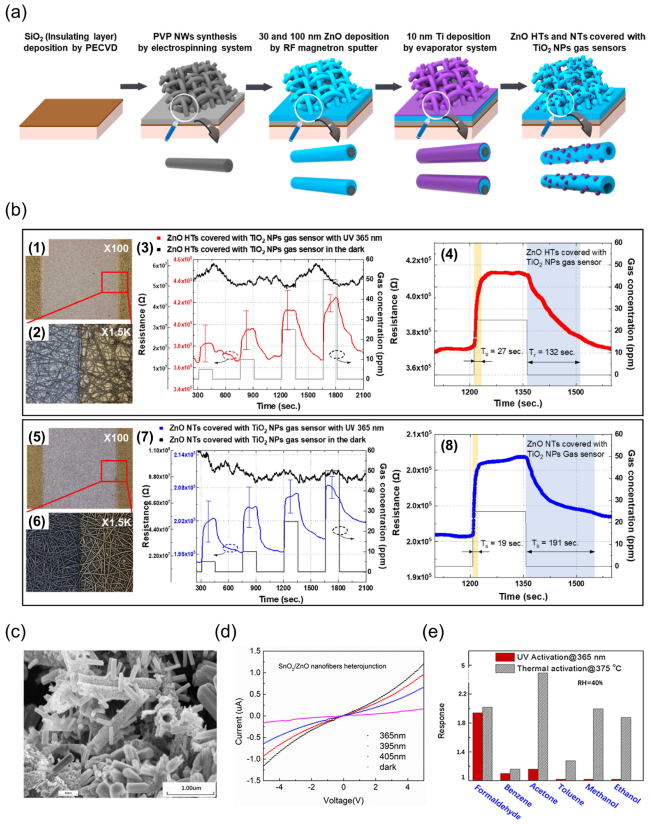

Fig. 3. (a) Fabrication of gas sensors consisting of ZnO hemitubes (HTs) and nanotubes (NTs) covered with TiO_2 nanoparticles (NPs). (b) (1, 5) Confocal microscopy images of gas sensors consisting of ZnO HTs and ZnO NTs covered with TiO_2 NPs, respectively; (2, 6) high magnification images; (3) resistance of ZnO HTs and ZnO NTs covered with TiO_2 NPs gas sensors in response to different NO_2 concentrations with and without UV illumination, respectively; (4, 8) resistance of ZnO HTs and ZnO NTs covered with TiO_2 NPs gas sensors to 25 ppm of NO_2, respectively. Reprinted with permission from Ref. [28] © 2020 by the authors. Licensee: MDPI, Basel, Switzerland. (c) Scanning electron microscope (SEM) images of the SnO_2/ZnO composite heterojunction. (d) I–V polarization curves of the SnO_2/ZnO composite heterojunction material under different light sources. (e) Comparison of the response of the SnO_2/ZnO heterojunction-based sensor to HCHO with other potential interferences, each at 50 ppm, under 365 nm light illumination, and with humidity at RH = 40%. Reprinted with permission from Ref. [29] © 2019 Li, Gu, Yang, Du, and Li.

nanotubes (NTs). Figs. 3 (b)-(1), (2), and (5), (6) show the structures of ZnO HTs and ZnO NTs, respectively, revealing that ZnO NTs possess a higher density than ZnO HTs. This structural difference allows the detection of resistance changes in the gas sensor owing to the multinetwork semiconductor material. The response of the sensor to varying concentrations of NO_2 gas under 365 nm UV light and dark conditions was tested (Figs. 3 (b)-(3), (7)). The ZnO HTs exhibited responses of 105, 108, 123, and

116% at NO_2 concentrations of 5, 10, 25, and 50 ppm, respectively (Fig. 3 (b)-(3)). In contrast, the response of ZnO NTs was lower at the same concentration (Fig. 3 (b)-(7)).

The higher gas sensitivity of ZnO HTs can be attributed to two main factors. First, ZnO HTs have more oxygen vacancy-related defects than ZnO NTs, providing more active sites for gas interactions and enhancing gas sensitivity [23-25]. This structure allowed oxygen ions to adsorb and desorb more easily. Second, the thinner walls of ZnO HTs result in a larger depletion layer and higher sensitivity [26]. Consequently, the sensors made from ZnO HTs exhibited a response 1.2 times higher than those made from ZnO NTs at 25 ppm NO_2. However, the sensors did not respond to room temperature (~22°C) without UV illumination. The gas-sensing characteristics of 25 ppm NO_2 were further examined (Figs. 3 (b)-(4), (8)). The response and recovery times for the ZnO-HT gas sensors were 27 and 132 s, respectively (Fig. 3 (b)-(4)), whereas those for the ZnO-NT gas sensors were 19 and 191 s, respectively (Fig. 3 (b)-(8)). Although the ZnO HTs have a faster overall gas response, their recovery time is longer than that of the ZnO NTs. The higher density and grain boundary density of the ZnO NTs led to a slower gas response than that of the ZnO HTs, which have a lower density. Thus, a high surface area and low grain boundary density can enhance the sensitivity of gas sensors [27].

Fig. 3 (c) shows the porous microstructure of the composite SnO_2/ZnO heterojunction nanofibers. The I-V polarization curves of these nanofibers were examined at different wavelengths (365, 395, and 405 nm) and in the dark (Fig. 3 (d)). The photocurrent increases as the wavelength decreases. Fig. 3 (e) presents the sensor response of SnO_2/ZnO nanofibers to 50 ppm of formaldehyde (HCHO), benzene (C_6H_6), $(CH_3)_2CO$, toluene ($C_6H_5CH_3$), methanol (CH_3OH), and C_2H_5OH under UV irradiation and at a high temperature of 375°C. In the absence of light, the sensor exhibited a strong response to $(CH_3)_2CO$ at 375°C, indicating the low selectivity. However, under UV irradiation at room temperature (~22°C), the sensor exhibited a high response to HCHO with improved selectivity to the gas. This suggests that UV activation allows the sensor to operate effectively at room temperature (~22°C) while maintaining a high selectivity.

3.3 2-Dimensional Photoactive Sensing Materials

As discussed above, zero-dimensional (0D) and one-dimensional (1D) nanostructures exhibit significant potential as photoactive sensors. However, their long-term stability remains a

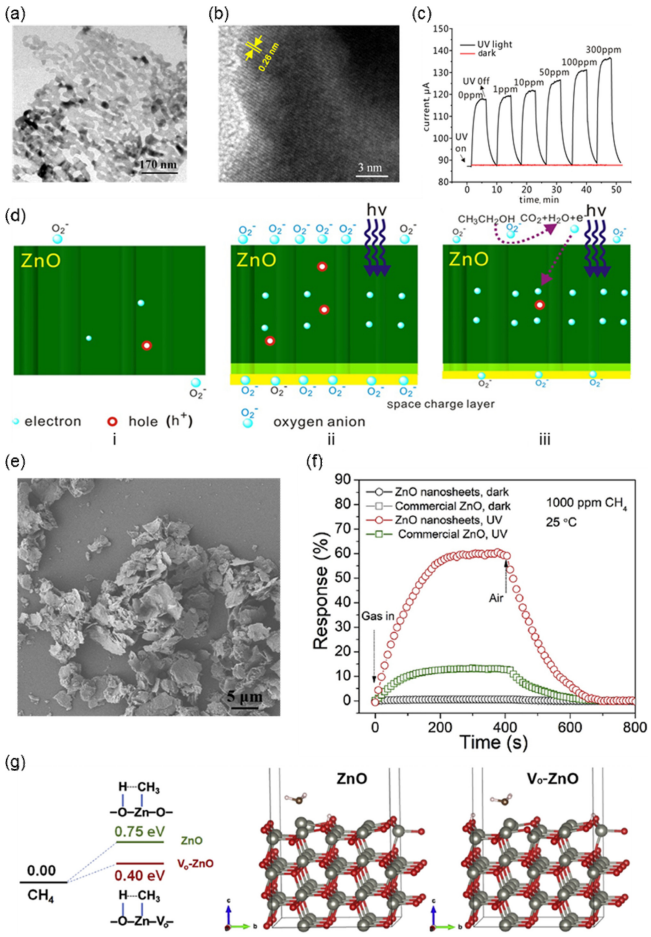

Fig. 4. (a) TEM image of PSC ZnO nanosheet and (b) HRTEM image of PSC ZnO nanosheet (c) Sensor responses to different C_2H_5OH concentrations under UV light. (d) UV-activated sensing mechanism. Reprinted with permission from Ref. [34] ©2017 The Institution of Engineering and Technology. (e) SEM image of the δ-$Zn(OH)_2$ precursor. (f) Sensing response profiles of the sensors fabricated from ZnO nanosheets and commercial ZnO to 1000 ppm (0.1%) of CH_4 in the dark and under UV irradiation. (g) Gibbs free energy diagrams for CH_4 dissociation on ZnO slab with and without oxygen vacancies. Reprinted with permission from Ref. [35] © 2021 Elsevier B.V. All rights reserved.

challenge. To overcome this problem, Meng et al. developed a gas-sensing material based on two-dimensional (2D) nanosheets. Specifically, they used porous single-crystalline (PSC) nanosheets as the active layer in a gas sensor to improve both the sensitivity and long-term stability [30]. Figs. 4 (a)-(d) illustrate the development of a ZnO gas sensor based on PSC activated by UV light at room temperature (~22°C). The transmission electron microscope (TEM) images of the PSC ZnO nanosheets reveal their porous structure (Fig. 4 (a)), while the high-resolution TEM (HRTEM) images show a consistent lattice pattern across the nanosheets (Fig. 4 (b)). Under UV irradiation, Fig. 4 (c) presents

the response of the sensor to various C_2H_5OH concentrations at room temperature (~22°C) under UV irradiation. In the absence of light, the sensor showed a minimal response to C_2H_5OH, whereas under UV exposure, a pronounced electric-current response was observed. This performance surpasses that of previously reported 1D UV-activated ZnO nanofiber sensors at room temperature (~22°C) [31,32]. This superior response was attributed to the larger contact area with the gas molecules in the 2D nanostructures and the increased number of active sites provided by the PSC structure.

Fig. 4 (d) shows the UV activation mechanism of the PSC ZnO nanosheets. ZnO, an n-type semiconductor with electrons as charge carriers, adsorbs oxygen onto its surface (Fig. 4 (d)-i). UV irradiation generates photoelectrons and holes, with the photoelectrons captured by the adsorbed oxygen, forming O_2^- (Fig. 4 (d)-ii). This decreases the number of surface electrons, deepens the depletion layer, and reduces surface conductivity. When C_2H_5OH molecules were introduced, they reacted with the oxygen anions, releasing the captured electrons back into ZnO (Fig. 4 (d)-iii). This resulted in a reduced depletion-layer depth and increased surface conductivity. Consequently, UV activation enhances the response of the sensor to the target gases, reduces power consumption, and improves its stability against flammable and explosive gases.

Figs. 4 (e)-(g) further illustrate the enhanced methane (CH_4) sensing characteristics of the nanosheet structures due to the incorporation of abundant surface oxygen vacancies (V_o) and improved photoactivation. Mesoporous ZnO nanosheets were synthesized from δ-$Zn(OH)_2$ nanosheets via thermal conversion at 200°C (Fig. 4 (e)). The sensing performance of the mesoporous ZnO nanosheets was compared with that of commercial ZnO nanoparticles under both dark and UV-irradiated conditions with 1,000 ppm CH_4 (Fig. 4 (f)). In the dark, both sensors showed no response; however, under UV light, a response was observed, with the mesoporous ZnO nanosheets exhibiting a higher sensitivity relative to commercial ZnO nanoparticles. This improved sensitivity was attributed to the higher surface area and enhanced charge separation from V_o [33]. Fig. 4 (g) shows the CH_4-dissociation energy barriers and diagrams for the ZnO (100) surface with and without surface V_o. It was found that the Gibbs free energy for CH_4 dissociation is 0.35 eV lower on ZnO slabs with V_o compared to those without V_o. The presence of abundant V_o on the mesoporous ZnO nanosheets facilitates the formation of Zn^+/O^- pairs and promotes the dissociation of CH_4 into CH_3 and H, enhancing photocatalytic oxidation and resulting in higher detection performance under UV illumination. These findings underscore the importance of the crystal structure, surface area, and presence of V_o in influencing the photoactivity and sensitivity of gas sensors.

3.4 3-Dimensional Photoactive Sensing Materials

As previously noted, extensive research has been conducted on photoactive gas sensors across the zero, one, and two dimensions, focusing on achieving high gas sensitivity under photoactivation at low temperatures. However, studies emphasizing structural features to maximize photoelectron properties remain limited in terms of uniformity and light utilization [36-42]. Fig. 5 demonstrates that the highly ordered three-dimensional (3D) porous TiO_2 nanostructures utilize multiple scattering effects to enhance light utilization and exhibit a superior gas response. The 3D TiO_2 structures were fabricated on Pt interdigitated electrodes using the proximity-field nanopatterning technology [43] (Fig. 5 (a)). Fig. 5 (b) shows the gas-response differences among various TiO_2 structures—pristine film (PF), colloidal particle (CP), inverse opal (IO), and 3D structures—under exposure to 50 ppm $(CH_3)_2CO$ at 400°C. The PF and CP structures exhibit minimal responses owing to limited gas access, whereas the IO structure shows significantly improved sensitivity as gases can reach the bottom of the nanostructures. The 3D TiO_2 structure further enhanced the gas response owing to its optimized interneck thickness and complete gas access to its base, demonstrating a higher gas reactivity owing to its periodic structure.

Fig. 5 (c) illustrates the NO_2 gas-sensing system under UV LED illumination. Figs. 5 (d) and 5 (e) highlight three critical aspects of the 3D TiO_2 structure with 600 nm periodicity. Fig. 5 (d) presents the i) utility factor and ii) transducer function. The body-centered tetragonal unit cell of 3D TiO_2 comprises a hollow ellipsoid core connected by eight internecks, facilitating gas access to both the internal and external surfaces ((i) utility factor) [44]. The hollow tubular structure significantly enhanced the collision frequency of NO_2 gas molecules. These eight internecks narrow the conduction channels because of the formation of a Schottky junction in the depletion layer created by ionized oxygen adsorption ((ii) transducer function) [45]. Fig. 5 (e) shows that additional light scattering by the 3D nanostructures maximizes the photoactivity, leading to the generation of numerous photoelectron-hole pairs ((iii) receptor function). Figs. 5 (f) and 5 (g) compare the responses of planar TiO_2 thin films and 3D TiO_2 structures to 5 ppm NO_2 at room temperature (~22°C) under UV and dark conditions, respectively. The planar TiO_2 films showed a minimal response in darkness and a slight increase under UV

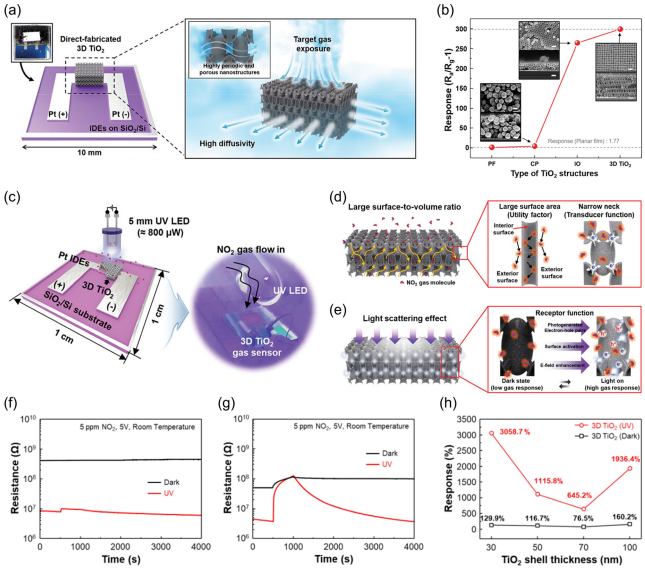

Fig. 5. (a) Directly fabricated 3D TiO_2 on interdigitated electrodes showing highly periodic and porous nanostructures. (b) Gas-sensing properties of various TiO_2 nanostructures. Gas responses of different TiO_2 configurations (PF: pristine film, CP: colloidal particle, IO: inverse-opal, 3D TiO_2) toward 50 ppm CH_3COCH_3 at 400°C. Reprinted with permission from Ref. [46] © 2021 Wiley-VCH GmbH. (c) 3D TiO_2 on Pt IDEs patterned on SiO_2/Si substrates, along with the gas-sensing measurement system. (d) Highly periodic TiO_2 nanonetworks for effective NO_2 gas permeation and (e) light-scattering effects induced by 3D nanostructures that enhance the electromagnetic field of the incident UV light. Resistance change plots of (f) planar TiO_2 thin film and (g) 3D TiO_2 with and without UV illumination. (h) Gas responses of 3D TiO_2 as a function of the TiO_2 thin-shell thickness with and without UV illumination. Reprinted with permission from Ref. [11] © 2020 The Authors. Published by Wiley VCH GmbH.

illumination (Fig. 5 (f)), whereas the 3D TiO_2 structures demonstrated a notable response even in darkness, with significantly enhanced sensitivity under UV light (Fig. 5 (g)). The base resistance also decreases under UV irradiation owing to the generation of photoelectron-hole pairs. This indicates that the high surface area and periodicity of the 3D TiO_2 structure contributed to the maximized photoactivity and improved gas response. However, when the shell thickness of 3D TiO_2 exceeded 70 nm, the gas response decreased because of the reduced porosity, although it improved beyond this thickness (Fig. 5 (h)). This suggests that below 70 nm, the gas response is more influenced by the porosity, whereas above 70 nm, light-scattering effects dominate. Thus, both structural dimensions and photoactivation levels are crucial for effective gas sensing.

The inherent issue of low selectivity in semiconductor oxide-based gas sensors can be addressed using strategies such as decorating the surface of the sensing materials with catalytic nanoparticles or coating them with gas-filtering membranes that possess pores specifically designed to selectively permit only target gas molecules to pass through. Fig. 6 presents a strategy for improving the gas selectivity of the 3D-nanostructured sensing layers. In general, photoactive nanomaterials (e.g., ZnO, TiO_2, and titanium nitride (TiN)) enhance the decomposition performance and chemical sensing capabilities [47-50]. However, the random aggregation of nanostructures can reduce device durability and reproducibility. Fig. 6 (a) illustrates a potential solution for fabricating 3D TiO_2 with highly active nanocatalysts to enhance electrochemical reactions. The 3D TiO_2 was decorated with metal-ion precursors (platinum $(Pt)^{2+}$, palladium $(Pd)^{2+}$, nickel $(Ni)^{2+}$, and cobalt $(Co)^{2+}$) which can be transformed into polyelemental forms through an active photothermal effect when treated with intense pulsed light. The formation of nanosized, polyelemental nanocatalysts was attributed to the controlled coating of the precursors and rapid thermal treatments to minimize nanoparticle agglomeration and overcome instability due to their high surface energy. Figs. 6 (b)-(d) compare the gas responses toward common volatile organic compounds at 10 ppm under 5 V with and without metal nanoparticles. Fig. 6 (b) shows that the 3D TiO_2 without metal nanoparticles responded well to most gases, except C_6H_6 but lacked selectivity for specific gases. After stabilizing the Pt and PtPd nanoparticles on the surface, a slight increase in the response to NO_2, H_2S, and C_3H_6O was observed; however, no significant improvements were noted. The addition of Ni improved the selectivity for hydrogen sulphide (H_2S) by accelerating the dissociation of chemically bonded oxygen species (O^{2-}, O^-, O_2^-) on the TiO_2 surface (Fig. 6 (d)), demonstrating that the selectivity can be adjusted by varying the type of precursor used.

Fig. 6 (e) shows the hierarchical nanostructures (HNS) of 3D ZnO/ZIF-8, where a ZIF-8 layer is coated on a ZnO thin shell. This configuration provides additional light scattering effects and enhances gas selectivity due to the micro- and nanoscale pores (3.4 Å) of ZIF-8. Fig. 6 (f) shows SEM images of the 3D ZnO/ZIF-8 HNS, which retained a periodically ordered structure despite the ZIF-8 coating. The TEM images confirm the uniform formation of a ZIF-8 layer on the ZnO film surface. Fig. 6 (g) shows the changes in gas selectivity with varying ZIF-8 thickness under UV illumination at room temperature (~22°C). NO_2, C_2H_5OH, $(CH_3)_2CO$, and $C_6H_5CH_3$ gases have molecular diameters of 3.3, 4.3, 4.7, and 5.7 Å [51,52], respectively. With a ZIF-8 pore size of 3.4 Å [53], the sensor shows the highest selectivity for NO_2, with a concentration of 0.1 ppm compared to 1 ppm for other gases. This demonstrates that NO_2, which is smaller than the ZIF-8 pores, exhibits higher reactivity.

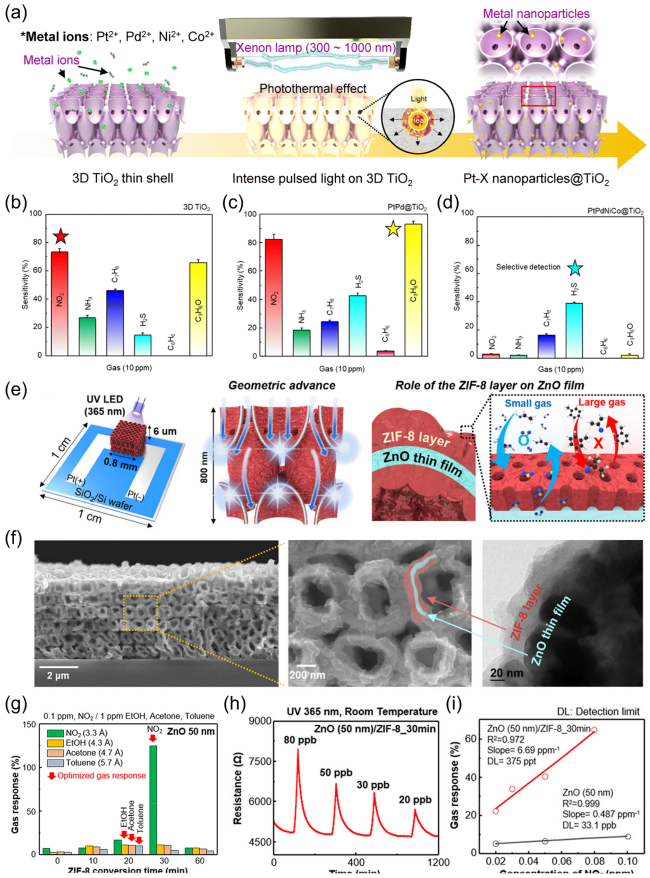

Fig. 6. (a) PtPdNiCo NPs@TiO_2 fabrication process driven by the intensive pulsed-light (IPL) method. Calculated responses (sensitivity) of (b) 3D TiO_2, (c) PtPd@TiO_2, and (d) PtPdNiCo@TiO_2 to six different gases: NO_2, ammonia, H_2S, C_6H_6, and C_3H_6O. Reprinted with permission from Ref. [54] © The Royal Society of Chemistry 2023. (e) 3D ZnO/ zeolitic-imidazolate frameworks (ZIF-8) hierarchical nanostructures (HNS) on Pt IDEs patterned on SiO_2/Si substrates, the geometric advantages of 3D ZnO/ZIF-8 HNS for detecting gas molecules, and the conceptualization of the role of the ZIF-8 layer on the ZnO film. (f) Cross-sectional SEM and TEM images of the fabricated 3D ZnO/ZIF-8 HNS (ZnO thin-shell thickness: 50 nm, ZIF-8 conversion time: 30 min). (g) Gas-selectivity analysis of 3D ZnO/ZIF-8 HNS with different ZIF-8 conversion times (ZnO film thickness: 50 nm). (h) Sensing performance of 3D ZnO (50 nm)/ZIF-8_30 min toward different concentrations of NO_2. (i) Linear fit of the responses as a function of NO_2 concentration. Reprinted with permission from Ref. [55] © 2023. The small Structures were published by Wiley-VCH GmbH.

Additionally, the sensor exhibited a theoretical detection limit of 375 parts-per-trillion (ppt) at low concentrations, indicating that the ZIF-8 layer enables detection below ppb levels (Fig. 6 (i)). Overall, 3D structures not only provide more active sites and utilize light more efficiently because of enhanced scattering but also enhance the sensitivity and selectivity of gas sensors by decorating with metal nanoparticles or coating with additional molecular sieving layers.

In this section, we briefly discussed the impact of structural dimensions on photoactivated gas sensors, emphasizing the critical role that dimensionality plays in determining the performance and efficiency of these devices. As the structure transitions from 0D to 3D, there is a marked improvement in the light absorption, gas interaction, and overall gas responses. While 0D materials such as quantum dots provide high sensitivity owing to their large surface area, they face challenges in terms of light utilization and gas accessibility. Conversely, 3D structures such as porous nanostructures can be beneficial for optimizing light scattering and surface area, leading to a significantly enhanced gas-sensing performance, particularly when working at lower power levels. The incorporation of metal nanoparticles and advanced nanostructuring further boosts photoactive properties, resulting in highly selective and sensitive gas sensors. These findings highlight the importance of tailoring structural dimensions to optimize photoactivation, paving the way for more efficient, low-power, and high-performance gas-sensing technologies.

4. UV μLED INTEGRATED GAS SENSORS

The previous section discussed the photoactivity and selectivity improvements that result from structural modifications. In addition, the adoption of UV micro-LEDs (μLEDs) for light irradiation has facilitated gas detection with substantially lower power consumption compared to conventional lamps or commercial LEDs [56,57]. These μLEDs present a viable alternative to traditional microheater-based methods, which require milliwatt-level power, involve complex fabrication [58,59], and are associated with high costs and safety risks due to material degradation [60]. As discussed previously, photoactivated sensing technologies allow the detection of gases at room temperature (~22°C), thereby mitigating thermal damage to the sensor platform. Photon irradiation enhances the sensor sensitivity and gas adsorption by increasing the generation of electron-hole pairs on the surfaces of semiconductor metal oxides (SMOs), thereby promoting redox reactions [56,57]. Future advancements will likely focus on combining UV technologies with highly selective gas sensors to further reduce power consumption and sensor size [61-63]. With their compact dimensions (< (100 × 100) μm²), high luminous efficiency, portability, stability, and rapid response times, μLEDs are emerging as key technologies for applications in next-generation displays, optical communications,

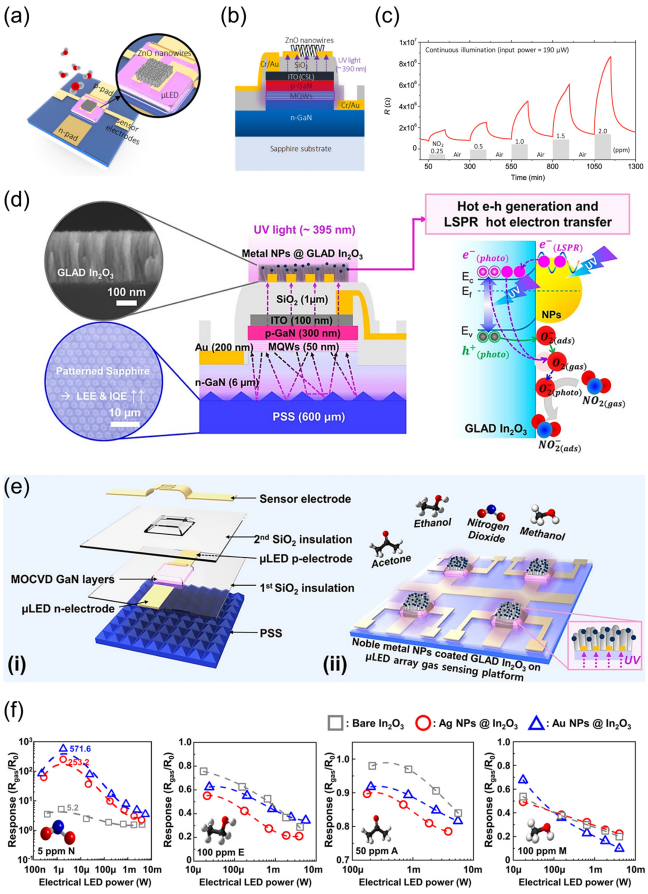

Fig. 7. Proposed monolithic photoactivated gas sensors on a μLP: (a) top view and (b) cross-sectional view. (c) 0.25–2 ppm NO_2 sensing performance of the photoactivated gas sensor on 30-μLP. All tests were conducted under an operating power of ~190 μW. Reprinted with permission from Ref. [61] © 2020 American Chemical Society. (d) Structure and sensing mechanism of the UV μLED gas sensor. (e) 3D images of (i) the laminated structure of the μLED gas sensing platform and (ii) GLAD In_2O_3 coated with noble metal NPs deposited on the μLED array platform. (f) Gas responses at various μLED powers for 5 ppm NO_2 (N), 100 ppm C_2H_5OH (E), 50 ppm $(CH_3)_2CO$ (A), and 100 ppm CH_3OH (M). Reprinted with permission from Ref. [80] © 2022 American Chemical Society.

and biomedicine [64-68].

Fig. 7 (a) outlines the schematic structure of a μLED-based photoactive gas sensor, which includes two p-n contact electrodes to drive the μLEDs and two cross or parallel electrodes to measure the gas-sensing signals. The μLED platform (μLP) features a peak-emission wavelength of 390 nm, and various emission-area structures were designed to analyze how LED size affects power efficiency and detection performance. Fig. 7 (b) shows the cross-sectional structure of a monolithic, photoactive sensor based on gallium nitride (GaN) μLEDs. In this structure, a 200 nm thick indium tin oxide layer is applied to the p-GaN layer for the ohmic contact. Electrical insulation between the LED and sensor electrodes was achieved using a 500 nm thick silicon dioxide (SiO_2) layer deposited via chemical vapor deposition. The sensing material used was sequentially synthesized ZnO nanowires, chosen for their excellent gas diffusion, superior photocatalytic properties, low electronic bandgap, and simple synthesis process [69-71]. The bandgap of ZnO is 3.2 eV at room temperature (~22°C), with an emission wavelength of approximately 387 nm, which matches the emission wavelength of the designed μLEDs [56]. The μLEDs are fabricated using precision micro-fabrication techniques. Fig. 7 (c) demonstrates the testing of NO_2 gas using a 30-μLP setup. Testing was conducted at an optimal operating power close to approximately 190 μW. The results exhibit clear detection responses and excellent recovery characteristics across a range of NO_2 gas concentrations from 0.25 to 2 ppm, highlighting the superior performance of the 30-μLP sensor.

Figs. 7 (d) and (e) further illustrate the development of an ultra-low-power e-nose system based on multiple UV-μLED gas sensors. Fig. 7 (d) shows the fabrication of μLEDs using a 395 nm wavelength ultraviolet-emitting GaN sapphire wafer, with a dual SiO_2 insulating layer applied to prevent electrical shorting. To maximize the light-extraction efficiency and internal quantum efficiency of LEDs, patterned sapphire substrate technology has been introduced [72]. Various μLED sizes were analyzed, leading to the selection of an optimized 50 × 50 μm^2 μLED. Porous nanocolumnar In_2O_3 films were deposited onto the μLEDs using the glancing-angle-deposition (GLAD) process for use as gas-sensing materials. To further enhance the performance of the photoactive gas sensors, plasmonic noble-metal NPs were coated onto the GLAD In_2O_3 surface via e-beam evaporation.

Fig. 7 (d) (right) describes the NO_2 gas-sensing mechanism under μLED illumination. In dark conditions, oxygen molecules (O_2) adsorb onto the metal oxide surface to form oxygen ions (O_2^-). Upon exposure to light with wavelengths between 250 and 450 nm, photo-generated electron-hole pairs ($e^-_{(photo)}$–$h^+_{(photo)}$) are created, significantly increasing charge density and electrical conductivity [73]. The photogenerated holes ($h^+_{(photo)}$) react with the adsorbed oxygen ions ($O_{2(ads)}^-$) to release oxygen molecules (O_2). These released oxygen molecules react with the photogenerated electrons to form more reactive photoadsorbed oxygen ions ($O_{2(photo)}^-$). When oxidative gases such as NO_2 approach, they either capture electrons from the photoadsorbed oxygen ions or directly from the conduction band of the metal oxide, leading to increased resistance as the electron concentration decreases [33]. The photogenerated electron-hole pairs activate the reactive sites on the semiconductor metal-oxide surface,

accelerating the adsorption of NO_2 and desorption of O_2 and significantly enhancing the sensor response and recovery rates. Additionally, the LSPR phenomenon [74-77] induced by plasmonic NPs generates strong electric fields and energetic electrons, further improving sensor responsiveness and recovery rates by providing additional charge carriers [78]. Fig. 7 (e) illustrates the layered structure of the LED gas sensor and a 3D schematic of the sensor chip. The single sensor chip features a 2 × 2 array of four μLEDs, emitting UV light from the bottom, which enhances interaction with the gas-detection material. The bottom illumination method improves gas detection by increasing the concentration of photogenerated electrons near the GLAD In_2O_3 nanocolumns, leading to shorter travel paths, reduced resistance, and faster response and recovery rates [79]. Fig. 7 (f) analyzes the gas responses of various gases in relation to the μLED power, aiming to determine the optimal operating conditions and evaluate the impact of metal NP coatings on gas-sensor performance. The experiment examined the μLED power variation for 5 ppm NO_2, 100 ppm C_2H_5OH, 50 ppm $(CH_3)_2CO$, and 100 ppm CH_3OH. Oxidative gases, such as NO_2 draw electrons from the surface of In_2O_3, reducing conductivity [33], while reducing volatile organic compounds (VOCs), such as C_2H_5OH, $(CH_3)_2CO$, and CH_3OH, which react with oxygen ions and increase conductivity. For NO_2, the maximum response was observed at an intermediate power of 1 μW, whereas the response of VOC gases increased monotonically with higher μLED power. However, when μLED power exceeded 1 μW, the response to NO_2 decreased, and VOC gases similarly showed a bell-shaped response trend. Specifically, at 1 μW, the gas response for 5 ppm NO_2 was 5.2 for bare In_2O_3, 253.2 for Ag NP-coated In_2O_3, and 571.6 (R_{gas}/R_0) for Au NP-coated In_2O_3, demonstrating that metal NP coatings increased the gas response by more than 100 times. The NP-coated sensors generally exhibited higher responses to VOC gases.

The optimal μLED operating condition was a 3.0 V forward bias, which enabled the detection of both oxidative and reductive gases, with a total sensor power consumption of only 0.38 mW. The μLED-based e-nose system proposed in this study demonstrates significant performance improvements over conventional heater-based systems through ultra-low power consumption and high sensitivity. The integration of μLEDs with gas sensors maximizes energy efficiency and opens new possibilities for mobile applications in Internet-of-Things (IoT) technology. Additionally, the small UV-emission area and room-temperature (~22°C) operation of LEDs make the system environmentally friendly and minimize the impact on users and their surroundings, highlighting the potential of LED integration as a key element in next-generation, ultralow-power IoT systems.

In this section, we discussed the integration of UV μ-LEDs in gas sensors, highlighting their role in achieving ultralow-power consumption while enhancing photoactivity and selectivity. The development of an e-nose system based on multiple UV-μLED gas sensors demonstrates significant advancements over traditional systems, including improved light absorption, gas interaction, and sensor responsiveness. The integration of metal nanoparticles and nanostructuring techniques, such as GLAD In_2O_3 films, further enhances their photoactive properties, leading to highly selective and sensitive gas sensors. The μLEDs, with their small UV emission area and room-temperature (~22°C) operation, offer an environmentally friendly and energy-efficient solution for gas sensors in mobile IoT applications.

5. CONCLUSIONS

With growing global emphasis on energy efficiency, the demand for gas sensors with high sensitivity, selectivity, and low-power operation is rapidly increasing [81]. To meet these requirements, research on photoactivated chemiresistors, particularly those based on metal-oxide semiconductors, has intensified. However, longstanding challenges such as insufficient sensitivity at near-room temperatures (~22°C) and poor stability against humidity remain unresolved. Nanostructuring has emerged as a key strategy to address these issues with the development of advanced nanostructures such as nanoparticles, nanowires, nanorods, and highly periodic 3D architectures, which play a pivotal role in enhancing the surface area and improving the sensor response capabilities. Additionally, advanced techniques such as catalytic doping, heterostructure formation, and hybridization have been extensively explored to revolutionize the sensor performance. The integration of these innovative nanostructuring approaches with micro-LED technology paves the way for the development of ultralow-power, high-performance gas sensors—positioning them as promising solutions for future practical and diverse applications. Therefore, continued research on these materials and technologies is expected to drive transformative advancements toward the realization of next-generation energy-efficient gas sensors. This review provides a comprehensive overview of recent research trends in these areas and proposes potential directions for future research.

ACKNOWLEDGMENTS

S. L., G. H. L., and M. C. contributed equally to this study. This study was supported by the Korea Research Institute of Chemical Technology (KRICT) Republic of Korea (KS2321-10). This work was also supported by the National Research Foundation of Korea (NRF) grant funded by the Korean Government (Ministry of Science and ICT) (RS-2024-00421857).

REFERENCES

[1] A. Mirzaei, S. Leonardi, and G. Neri, "Detection of hazardous volatile organic compounds (VOCs) by metal oxide nanostructures-based gas sensors: A review", *Ceram. Int.*, Vol. 42, No. 14, pp. 15119-15141, 2016.

[2] G. F. Fine, L. M. Cavanagh, A. Afonja, and R. Binions, "Metal oxide semi-conductor gas sensors in environmental monitoring", *Sens.*, Vol. 10, No. 6, pp. 5469-5502, 2010.

[3] X. Chen, M. Leishman, D. Bagnall, and N. Nasiri, "Nanostructured gas sensors: From air quality and environmental monitoring to healthcare and medical applications", *Nanomater.*, Vol. 11, No. 8, p. 1927, 2021.

[4] S. Uma and M. Shobana, "Metal oxide semiconductor gas sensors in clinical diagnosis and environmental monitoring", *Sens. Actuators A Phys.*, Vol. 349, p. 114044, 2023.

[5] E. Kanazawa, G. Sakai, K. Shimanoe, Y. Kanmura, Y. Teraoka, N. Miura, and N. Yamazoe, "Metal oxide semiconductor N_2O sensor for medical use", *Sens. Actuators B Chem.*, Vol. 77, No. 1-2, pp. 72-77, 2001.

[6] C. Wang, L. Yin, L. Zhang, D. Xiang, and R. Gao, "Metal oxide gas sensors: sensitivity and influencing factors", *Sens.*, Vol. 10, No. 3, pp. 2088-2106, 2010.

[7] A. Lahlalia, L. Filipovic, and S. Selberherr, "Modeling and simulation of novel semiconducting metal oxide gas sensors for wearable devices", *IEEE Sens. J.*, Vol. 18, No. 5, pp. 1960-1970, 2018.

[8] F. Sarf, "Metal oxide gas sensors by nanostructures", *Gas Sens.*, Vol. 1, pp. 1-17, 2020.

[9] H. Jin, T.-P. Huynh, and H. Haick, "Self-healable sensors based nanoparticles for detecting physiological markers via skin and breath: toward disease prevention via wearable devices", *Nano Lett.*, Vol. 16, No. 7, pp. 4194-4202, 2016.

[10] M. Šetka, M. Claros, O. Chmela, and S. Vallejos, "Photoactivated materials and sensors for NO_2 monitoring", *J. Mater. Chem. C*, Vol. 9, No. 47, pp. 16804-16827, 2021.

[11] D. Cho, J. M. Suh, S. H. Nam, S. Y. Park, M. Park, T. H. Lee, K. S. Choi, J. Lee, C. Ahn, H. W. Jang, Y.-S. Shim, and S. Jeon, "Optically activated 3D thin-shell TiO_2 for supersensitive chemoresistive responses: toward visible light activation", *Adv. Sci.*, Vol. 8, No. 3, p. 2001883, 2021.

[12] T. Seiyama, A. Kato, K. Fujiishi, and M. Nagatani, "A new detector for gaseous components using semiconductive thin films", *Anal. Chem.*, Vol. 34, No. 11, pp. 1502-1503, 1962.

[13] N. Taguchi, "Gas-detecting device", U. S. Patent US3631436A, 18 Dec., 1971.

[14] Y. Shi, L. Li, Z. Xu, F. Guo, and W. Shi, "Construction of full solar-spectrum available S-scheme heterojunction for boosted photothermal-assisted photocatalytic H_2 production", *J. Chem. Eng.*, Vol. 459, p. 141549, 2023.

[15] H. Zhao, Y. Wang, and Y. Zhou, "Accelerating the Gas–Solid Interactions for Conductometric Gas Sensors: Impacting Factors and Improvement Strategies", *Mater.*, Vol. 16, No. 8, p. 3249, 2023.

[16] G. Ghorbani and F. Taghipour, "UV-activated chemiresistive gas sensor response curve analysis for the fast measurement of toxic gases", *Sens. Actuators B Chem.*, p. 136396, 2024.

[17] I. Ahmad, P. S. Lo, A. Khaleed, A. Djurišic, Y. He, and A. M. C. Ng, "Metal oxide nanoparticles incorporated mesoporous silica nanospheres for oxygen scavenging", *Proc. of Oxide-based Materials and Devices XIII*, pp. 181-187, San Francisco, United States, 2022.

[18] M. S. Almomani, N. M. Ahmed, M. Rashid, N. Suardi, M. A. Almessiere, N. Madkhali, O. A. Aldaghri, and K. H. Ibnaouf, "Photovoltaic performance of spherical TiO_2 nanoparticles derived from titanium hydroxide $Ti(OH)_4$: role of annealing varying temperature", *Energies*, Vol. 15, No. 5, p. 1648, 2022.

[19] H. Liu, W. Shen, X. Chen, and J.-P. Corriou, "A high-performance NH_3 gas sensor based on TiO_2 quantum dot clusters with ppb level detection limit at room temperature", *J. Mater. Sci.: Mater. Electron.*, Vol. 29, pp. 18380-18387, 2018.

[20] U. Joost, A. Šutka, M. Visnapuu, A. Tamm, M. Lembinen, M. Antsov, K. Utt, K. Smits, E. Nõmmiste, and V. Kisand, "Colorimetric gas detection by the varying thickness of a thin film of ultrasmall PTSA-coated TiO_2 nanoparticles on a Si substrate", *Beilstein J. Nanotechnol.*, Vol. 8, No. 1, pp. 229-236, 2017.

[21] A. Šutka, R. Eglitis, A. Kuzma, K. Smits, A. Zukuls, J. D. Prades, and C. Fàbrega, "Photodoping-Inspired Room-Temperature Gas Sensing by Anatase TiO_2 Quantum Dots", *ACS Appl. Nano Mater.*, Vol. 4, No. 3, pp. 2522-2527, 2021.

[22] T. Thathsara, C. J. Harrison, D. Schönauer-Kamin, U. Mansfeld, R. Moos, R. Moos, F. M. Malherbe, R. K. Hocking, and M. Shafiei, "Pd Nanoparticles Decorated Hollow TiO_2 Nanospheres for Highly Sensitive and Selective UV-Assisted Hydrogen Gas Sensors", *ACS Appl. Energy Mater.*, Vol. 7, No. 14, pp. 5608-5620, 2024.

[23] M.-W. Ahn, K.-S. Park, J.-H. Heo, J.-G. Park, D.-W. Kim, K. J. Choi, J.-H. Lee, and S.-H. Hong, "Gas sensing properties of defect-controlled ZnO-nanowire gas sensor", *Appl. Phys. Lett.*, Vol. 93, No. 26, p. 263103, 2008.

[24] Q. Yu, C. Yu, J. Wang, F. Guo, S. Gao, S. Jiao, H. Li, X. Zhang, X. Wang, H. Gao, H. Yang, and L. Zhao, "Gas sensing properties of self-assembled ZnO nanotube bundles", *RSC Adv.*, Vol. 3, No. 37, pp. 16619-16625, 2013.

[25] S. Cho, D. H. Kim, B. S. Lee, J. Jung, W. R. Yu, S. H. Hong, and S. Lee, "Ethanol sensors based on ZnO nanotubes with controllable wall thickness via atomic layer deposition, an O_2 plasma process and an annealing process", *Sens. Actuators B Chem.*, Vol. 162, No. 1, pp. 300-306, 2012.

[26] G. Korotcenkov, "The role of morphology and crystallographic structure of metal oxides in response of conductometric-type gas sensors", *Mater. Sci. Eng. R Rep.*, Vol. 61, No. 1-6, pp. 1-39, 2008.

[27] N. Shaalan, T. Yamazaki, and T. Kikuta, "Influence of morphology and structure geometry on NO_2 gas-sensing characteristics of SnO_2 nanostructures synthesized via a thermal evaporation method", *Sens. Actuators B Chem.*, Vol. 153, No. 1, pp. 11-16, 2011.

[28] H. J. Choi, S. H. Kwon, W. S. Lee, K. G. Im, T. H. Kim, B. R. Noh, S. Park, S. Oh, and K.-K. Kim, "Ultraviolet photoactivated room temperature NO_2 gas sensor of ZnO hemitubes and nanotubes covered with TiO_2 nanoparticles", *Nanomater.*, Vol. 10, No. 3, p. 462, 2020.

[29] J. Li, D. Gu, Y. Yang, H. Du, and X. Li, "UV light activated SnO_2/ZnO nanofibers for gas sensing at room temperature", *Front. Mater.*, Vol. 6, p. 158, 2019.

[30] J. Liu, Z. Guo, F. Meng, T. Luo, M. Li, and J. Liu, "Novel porous single-crystalline ZnO nanosheets fabricated by annealing ZnS (en) 0.5 (en= ethylenediamine) precursor. Application in a gas sensor for indoor air contaminant detection", *Nat. Nanotechnol.*, Vol. 20, No. 12, p. 125501, 2009.

[31] J. Gong, Y. Li, X. Chai, Z. Hu, and Y. Deng, "UV-light-activated ZnO fibers for organic gas sensing at room temperature", *J. Phys. Chem. C.*, Vol. 114, No. 2, pp. 1293-1298, 2010.

[32] S. Park, S. An, Y. Mun, and C. Lee, "UV-enhanced NO_2 gas sensing properties of SnO_2-core/ZnO-shell nanowires at room temperature", *ACS Appl. Mater. Interfaces*, Vol. 5, No. 10, pp. 4285-4292, 2013.

[33] A. Dey, "Semiconductor metal oxide gas sensors: A review", *Mater. Sci. Eng. B.*, Vol. 229, pp. 206-217, 2018.

[34] F. Meng, H. Zheng, Y. Sun, M. Li, and J. Liu, "UV-activated room temperature single-sheet ZnO gas sensor", *Micro Nano Lett.*, Vol. 12, No. 10, pp. 813-817, 2017.

[35] J. Wang, C. Hu, Y. Xia, and B. Zhang, "Mesoporous ZnO nanosheets with rich surface oxygen vacancies for UV-activated methane gas sensing at room temperature", *Sens. Actuators B Chem.*, Vol. 333, p. 129547, 2021.

[36] J. Lee, M. Park, Y. G. Song, D. Cho, K. Lee, Y. S. Shim, and S. Jeon, "Role of graphene quantum dots with discrete band gaps on SnO_2 nanodomes for NO_2 gas sensors with an ultralow detection limit", *Nanoscale Adv.*, Vol. 5, No. 10, pp. 2767-2775, 2023.

[37] J. Lee, D. Cho, H. Chen, Y.-S. Shim, J. Park, and S. Jeon, "Proximity-field nanopatterning for high-performance chemical and mechanical sensor applications based on 3D nanostructures", *Appl. Phys. Rev.*, Vol. 9, No. 1, p. 011322, 2022.

[38] S. H. Nam, M. Kim, N. Kim, D. Cho, M. Choi, J. H. Park, J. Shin, and S. Jeon, "Photolithographic realization of target nanostructures in 3D space by inverse design of phase modulation", *Sci. Adv.*, Vol. 8, No. 21, p. eabm6310, 2022.

[39] S. H. Nam, G. Hyun, D. Cho, S. Han, G. Bae, H. Chen, K. Kim, Y. Ham, J. Park, and S. Jeon, "Fundamental principles and development of proximity-field nanopatterning toward advanced 3D nanofabrication", *Nano Res.*, Vol. 14, pp. 2965-2980, 2021.

[40] W. Ku, G. Lee, J. Y. Lee, D. H. Kim, K. H. Park, J. Lim, D. Cho, S. C. Ha, B. G. Jung, H. Hwang, W. Lee, H. Shin, H. S. Jang, J.-O. Lee, and J.-H. Hwang, "Rational design of hybrid sensor arrays combined synergistically with machine learning for rapid response to a hazardous gas leak environment in chemical plants", *J. Hazard. Mater.*, Vol. 466, p. 133649, 2024.

[41] D. Kwak, H. Kim, S. Jang, B. G. Kim, D. Cho, H. Chang, and J. O. Lee, "Investigation of Laser-Induced Graphene (LIG) on a Flexible Substrate and Its Functionalization by Metal Doping for Gas-Sensing Applications", *Int. J. Mol. Sci.*, Vol. 25, No. 2, p. 1172, 2024.

[42] J. M. Suh, Y. G. Song, J. H. Seo, M. S. Noh, M. G. Kang, W. Sohn, J. Lee, K. Lee, D. Cho, S. Jeon, C.-Y. Kang, Y.-S. Shim, and H. W. Jang, "Facile Formation of Metal–Oxide Nanocraters by Laser Irradiation for Highly Enhanced Detection of Volatile Organic Compounds", *Small Struct.*, Vol. 4, No. 9, p. 2300068, 2023.

[43] S. Jeon, J. U. Park, R. Cirelli, S. Yang, C. E. Heitzman, P. V. Braun, P. J. A. Kenis, and J. A. Rogers, "Fabricating complex three-dimensional nanostructures with high-resolution conformable phase masks", *Proc. of Natl. Acad. Sci.*, pp. 12428-12433, United States, 2004.

[44] A. Sanger, S. B. Kang, M. H. Jeong, M. J. Im, I. Y. Choi, C. U. Kim, H. Lee, Y. M. Kwon, J. M. Baik, H. W. Jang, and K. J. Choi, "Morphology-Controlled Aluminum-Doped Zinc Oxide Nanofibers for Highly Sensitive NO_2 Sensors with Full Recovery at Room Temperature", *Adv. Sci.*, Vol. 5, No. 9, p. 1800816, 2018.

[45] N. Barsan and U. Weimar, "Conduction model of metal oxide gas sensors", *J. Electroceram.*, Vol. 7, pp. 143-167, 2001.

[46] J. M. Suh, D. Cho, S. Lee, T. H. Lee, J. W. Jung, J. Lee, S. H. Cho, T. H. Eom, J. W. Hong, Y. S. Shim, S. Jeon, and H. W. Jang, "Rationally designed TiO_2 nanostructures of continuous pore network for fast-responding and highly sensitive acetone sensor", *Small Methods*, Vol. 5, No. 12, p. 2100941, 2021.

[47] M. Tobajas, C. Belver, and J. Rodriguez, "Degradation of emerging pollutants in water under solar irradiation using novel TiO_2-ZnO/clay nanoarchitectures", *J. Chem. Eng.*, Vol. 309, pp. 596-606, 2017.

[48] Y. Zhang, Z.-R. Tang, X. Fu, and Y.-J. Xu, "TiO_2− graphene nanocomposites for gas-phase photocatalytic degradation of volatile aromatic pollutant: is TiO_2− graphene truly different from other TiO_2− carbon composite materials?", *ACS Nano*, Vol. 4, No. 12, pp. 7303-7314, 2010.

[49] A. Mancuso, O. Sacco, V. Vaiano, D. Sannino, S. Pragliola, V. Venditto, and N. Morante, "Visible light active Fe-Pr co-doped TiO_2 for water pollutants degradation", *Catal. Today.*, Vol. 380, pp. 93-104, 2021.

[50] W.-K. Wang, W. Zhu, L. Mao, J. Zhang, Z. Zhou, and G. Zhao, "Two-dimensional TiO_2-g-C_3N_4 with both TiN and CO bridges with excellent conductivity for synergistic photoelectrocatalytic degradation of bisphenol A", *J. Colloid Interface Sci.*, Vol. 557, pp. 227-235, 2019.

[51] D. H. Kim, S. Chong, C. Park, J. Ahn, J. S. Jang, J. Kim,

and I.-D. Kim, "Oxide/ZIF-8 Hybrid Nanofiber Yarns: Heightened Surface Activity for Exceptional Chemiresistive Sensing", *Adv. Mater.*, Vol. 34, No. 10, p. 2105869, 2022.

[52] T. La Rocca, E. Carretier, D. Dhaler, E. Louradour, T. Truong, and P. Moulin, "Purification of pharmaceutical solvents by pervaporation through hybrid silica membranes", *Membranes*, Vol. 9, No. 7, p. 76, 2019.

[53] S. R. Venna and M. A. Carreon, "Highly permeable zeolite imidazolate framework-8 membranes for CO_2/CH_4 separation", *J. Am. Chem. Soc.*, Vol. 132, No. 1, pp. 76-78, 2010.

[54] J. Shin, G. Lee, M. Choi, H. Jang, Y. Lim, G. S. Kim, S. H. Nam, S. H. Baek, H. C. Song, J. Kim, C. Y. Kang, J.-O. Lee, S. Jeon, D. Cho, and J.-S. Jang, "Atomically mixed catalysts on a 3D thin-shell TiO_2 for dual-modal chemical detection and neutralization", *J. Mater. Chem. A.*, Vol. 11, No. 34, pp. 18195-18206, 2023.

[55] J. Lee, H. Lee, T. H. Bae, D. Cho, M. Choi, G. Bae, Y. S. Shim, and S. Jeon, "3D ZnO/ZIF-8 Hierarchical Nanostructure for Sensitive and Selective NO_2 Sensing at Room Temperature", *Small Structures*, Vol. 5, No. 4, p. 2300503, 2024.

[56] E. Espid and F. Taghipour, "UV-LED photo-activated chemical gas sensors: A review", *Crit. Rev. Solid State Mater. Sci.*, Vol. 42, No. 5, pp. 416-432, 2017.

[57] J. Saura, "Gas-sensing properties of SnO_2 pyrolytic films subjected to ultrviolet radiation", *Sens. Actuators B Chem.*, Vol. 17, No. 3, pp. 211-214, 1994.

[58] Y. Lim, S. Lee, Y. M. Kwon, J. M. Baik, and H. Shin, "Gas sensor based on a metal oxide nanowire forest built on a suspended carbon nano-heater", *Proc. of 2018 IEEE. Micro Electro Mechanical Systems (MEMS)*, pp. 905-907, Belfast, UK, 2018.

[59] G. Meng, F. Zhuge, K. Nagashima, A. Nakao, M. Kanai, Y. He, M. Boudot, T. Takahashi, K. Uchida, and Takeshi Yanagida, "Nanoscale thermal management of single SnO_2 nanowire: pico-joule energy consumed molecule sensor", *ACS Sens.*, Vol. 1, No. 8, pp. 997-1002, 2016.

[60] E. Espid and F. Taghipour, "Development of highly sensitive ZnO/In_2O_3 composite gas sensor activated by UV-LED", *Sens. Actuators B Chem.*, Vol. 241, pp. 828-839, 2017.

[61] I. Cho, Y. C. Sim, M. Cho, Y.-H. Cho, and I. Park, "Monolithic micro light-emitting diode/metal oxide nanowire gas sensor with microwatt-level power consumption", *ACS Sens.*, Vol. 5, No. 2, pp. 563-570, 2020.

[62] W. Hu, L. Wan, Y. Jian, C. Ren, K. Jin, X. Su, X. Bai, H. Haick, M. Yao, and W. Wu, "Electronic noses: from advanced materials to sensors aided with data processing", *Adv. Mater. Technol.*, Vol. 4, No. 2, p. 1800488, 2019.

[63] H. Chen, D. Huo, and J. Zhang, "Gas recognition in E-nose system: A review", *IEEE Trans. Biomed. Circuits Syst.*, Vol. 16, No. 2, pp. 169-184, 2022.

[64] H. Jiang and J. Lin, "Nitride micro-LEDs and beyond-a decade progress review", *Opt. Express.*, Vol. 21, No. 103, pp. A475-A484, 2013.

[65] T. Wu, C. W. Sher, Y. Lin, C. F. Lee, S. Liang, Y. Lu, S. W. H. Chen, W. Guo, H. C. Kuo, and Z. Chen, "Mini-LED and micro-LED: promising candidates for the next generation display technology", *Appl. Sci.*, Vol. 8, No. 9, p. 1557, 2018.

[66] P. Tian, J. J. D. McKendry, Z. Gong, B. Guilhabert, I. M. Watson, E. Gu, Z. Chen, G. Zhang, and M. D. Dawson, "Size-dependent efficiency and efficiency droop of blue InGaN micro-light emitting diodes", *Appl. Phys. Lett.*, Vol. 101, No. 23, p. 231110, 2012.

[67] F. Olivier, S. Tirano, L. Dupré, B. Aventurier, C. Largeron, and F. Templier, "Influence of size-reduction on the performances of GaN-based micro-LEDs for display application", *J. Lumin.*, Vol. 191, pp. 112-116, 2017.

[68] N. L. Ploch, H. Rodriguez, C. Stolmacker, M. Hoppe, M. Lapeyrade, J. Stellmach, F. Mehnke, T. Wernicke, A. Knauer, V. Kueller, M. Weyers, S. Einfeldt, and M. Kneissl, "Effective thermal management in ultraviolet light-emitting diodes with micro-LED arrays", *IEEE Trans. Electron Dev.*, Vol. 60, No. 2, pp. 782-786, 2013.

[69] Q. Wan, Q. H. Li, Y. J. Chen, T. H. Wang, X. L. He, J. P. Li, and C. L. Lin, "Fabrication and ethanol sensing characteristics of ZnO nanowire gas sensors", *Appl. Phys. Lett.*, Vol. 84, No. 18, pp. 3654-3656, 2004.

[70] Y. Sivalingam, E. Martinelli, A. Catini, G. Magna, G. Pomarico, F. Basoli, R. Paolesse, and C. Di Natale, "Gas-sensitive photoconductivity of porphyrin-functionalized ZnO nanorods", *J. Phys. Chem. C.*, Vol. 116, No. 16, pp. 9151-9157, 2012.

[71] L. Peng, J. Zhai, D. Wang, Y. Zhang, P. Wang, Q. Zhao, and T. Xie, "Size-and photoelectric characteristics-dependent formaldehyde sensitivity of ZnO irradiated with UV light", *Sens. Actuators B Chem.*, Vol. 148, No. 1, pp. 66-73, 2010.

[72] S.-H. Chao, L.-H. Yeh, R. T. Wu, K. Kawagishi, and S.-C. Hsu, "Novel patterned sapphire substrates for enhancing the efficiency of GaN-based light-emitting diodes", *RSC Adv.*, Vol. 10, No. 28, pp. 16284-16290, 2020.

[73] Qomaruddin, O. Casals, H. S. Wasisto, A. Waag, J. D. Prades, and C. Fàbrega, "Visible-light-driven room temperature NO_2 gas sensor based on localized surface plasmon resonance: the case of gold nanoparticle decorated zinc oxide nanorods (ZnO NRs)", *Chemosensors*, Vol. 10, No. 1, p. 28, 2022.

[74] C. Clavero, "Plasmon-induced hot-electron generation at nanoparticle/metal-oxide interfaces for photovoltaic and photocatalytic devices", *Nat. Photon.*, Vol. 8, No. 2, pp. 95-103, 2014.

[75] X.-C. Ma, Y. Dai, L. Yu, and B.-B. Huang, "Energy transfer in plasmonic photocatalytic composites", *Light Sci. Appl.*, Vol. 5, No. 2, pp. e16017-e16017, 2016.

[76] K. M. Mayer and J. H. Hafner, "Localized surface plasmon resonance sensors", *Chem. Rev.*, Vol. 111, No. 6, pp. 3828-3857, 2011.

[77] C. Wang and D. Astruc, "Nanogold plasmonic photocatalysis for organic synthesis and clean energy conversion", *Chem. Soc. Rev.*, Vol. 43, No. 20, pp. 7188-7216, 2014.

[78] X. Tian, X. Yang, F. Yang, and T. Qi, "A visible-light activated gas sensor based on perylenediimide-sensitized SnO_2 for NO_2 detection at room temperature", *Colloids Surf., A*, Vol. 578, p. 123621, 2019.

[79] X.-X. Wang, S. Zhang, Y. Liu, J.-N. Dai, H.-Y. Li, and X.

Guo, "Light-excited chemiresistive sensors integrated on LED microchips", *J. Mater. Chem. A.*, Vol. 9, No. 30, pp. 16545-16553, 2021.

[80] K. Lee, I. Cho, M. Kang, J. Jeong, M. Choi, K. Y. Woo, K. J. Yoon, Y. H. Cho, and I. Park, "Ultra-low-power e-nose system based on multi-micro-led-integrated, nanostructured gas sensors and deep learning", *ACS Nano*, Vol. 17, No. 1, pp. 539-551, 2022.

[81] J. Hwang, S.-H. Park, Y.-S. Shim, S. Sohn, J. H. Chung, Y.-H. Cho, J. Lee, M. Choi, G. H. Lee, D. Cho, K. Lee, and W. Lee, "Fast and selective isoprene gas sensor: influence of polystyrene size and role of the Au catalyst on gas sensing properties", *Sens. Actuators B Chem.*, Vol. 422, pp. 136500, 2024.